Effects of temperature-dependent burn-in decay on the performance of triple cation mixed halide perovskite solar cells

Yusuf A. Olanrewaju, Kingsley Orisekeh, Omolara V. Oyelade, et al.

View Online   Export Citation   CrossMark

ARTICLES YOU MAY BE INTERESTED IN

Call For Papers!

AIP Advances

SPECIAL TOPIC: Advances in Low Dimensional and 2D Materials

Effects of temperature-dependent burn-in decay on the performance of triple cation mixed halide perovskite solar cells

View Online   Export Citation   CrossMark

Yusuf A. Olanrewaju,[1] Kingsley Orisekeh,[1] Omolara V. Oyelade,[2] Richard K. Koech,[1] [ID] Reisya Ichwani,[3] Abraham I. Ebunu,[1] Daniel I. Amune,[1] [ID] Abdulhakeem Bello,[2] [ID] Vitalis C. Anye,[1] Oluwaseun K. Oyewole,[3,4] [ID] and Winston O. Soboyejo[3,4,5,a)] [ID]

AFFILIATIONS

[1] Department of Materials Science and Engineering, African University of Science and Technology, Km. 10 Airport Road, P. M. B. 681, Garki, Abuja, Federal Capital Territory, Nigeria

[2] Department of Theoretical and Applied Physics, African University of Science and Technology, Km 10 Airport Road, P. M. B. 681, Garki, Abuja, Federal Capital Territory, Nigeria

[3] Department of Mechanical Engineering, Worcester Polytechnic Institute, 100 Institute Road, Worcester, Massachusetts 01609, USA

[4] Program in Materials Science and Engineering, Department of Mechanical Engineering, Worcester Polytechnic Institute, 100 Institute Road, Worcester, Massachusetts 01609, USA

[5] Department of Biomedical Engineering, Worcester Polytechnic Institute, 60 Prescott Street, Gateway Park, Life Sciences and Bioengineering Center, Worcester, Massachusetts 01609, USA

a)**Current address:** Program in Materials Science and Engineering, Worcester Polytechnic Institute, 100 Institute Road, Worcester, Massachusetts 01609, USA. **Author to whom correspondence should be addressed:** wsoboyejo@wpi.edu. **Tel.:** +1 508 831 5448

ABSTRACT

The understanding of the degradation mechanisms in perovskite solar cells (PSCs) is important as they tend to degrade faster under exposure to heat and light conditions. This paper examines the temperature-dependent degradation of solution processed triple-cation mixed halide PSCs ($Cs_{0.05}(FA_{0.95}MA_{0.05})_{0.95}Pb(I_{0.9}Br_{0.05})3$). The PSCs were subjected to temperatures between 30 and 60 °C for 3 h (180 min) to evaluate their current–voltage performance characteristics. Temperature-induced changes in the layer and interfacial structure were also elucidated by scanning electron microscopy (SEM). Our results show that thermally induced degradation leads gradually to the burn-in decay of photocurrent density, which results in a rapid reduction in power conversion efficiency. The SEM images reveal thermally induced delamination and microvoid formation between the layers. The underlying degradation in the solar cell performance characteristics is associated with the formation of these defects (interfacial cracks and microvoids) during the controlled heating of the mixed halide perovskite cells. The electrochemical impedance spectroscopy analysis of the PSCs suggests that the device charge transport resistance and the interfacial capacitance associated with charge accumulation at the interfaces both increase with extended exposure to light.

I. INTRODUCTION

The photoconversion efficiencies of organic–inorganic halide perovskite (OIHP) solar cells have improved dramatically due to their unique combination of optoelectronic properties such as high absorption characteristics, tunable direct bandgaps, excellent bipolar carrier transport, and long charge diffusion lengths.[1–12] Their highest certified power conversion efficiency (PCE) of 25.2% was achieved during the past decade. Such rapid efficiency, which is comparable to that of commercial single crystal solar cells, has stimulated considerable interest in the future application of OIHPs. However, there are still major concerns about the stability of OIHPs

under exposure to heat and light.[13,14] Such exposure has been shown to degrade the current–voltage characteristics of OIHPs under environmental and electric field conditions that stimulate possible service conditions.[15–17]

Nevertheless, our current understanding of the mechanism of OIHP degradation is still limited, although it is well known that exposure to moisture, oxygen, irradiation, and elevated temperatures[16,18–23] results in significant reductions in OIHP performance/durability. They are major impediments to their large-scale/industrial commercialization, despite the attractive PCEs that have been reported for OIHP solar cells with the use of methylammonium lead iodide (MAPbI$_3$)[24] and other absorber layers containing formamidinium, bromide, and chloride.[25–28] Encapsulation has also been used to limit moisture penetration, which also reduces the evaporation of volatile components in perovskite absorbers.[29–31]

The evolution of stability is closely linked with ABX$_3$ perovskite structures (where A = organic cation, B = divalent metal such as Pb, and X = halide ion). Pure MAPbX$_3$ and FAPbX$_3$ perovskite compounds are easy to degrade since they undergo strong temperature-induced decomposition[32] in inorganic and organic compounds. The final products of decomposition also depend on temperature.[33,34] Enhancements in the thermal stability of the perovskite have also been achieved by the use of more complex and varied mixtures of A$^-$, B$^-$, and X$^-$ site compositions (such as the mixture of both methylammonium and formamidinium as the monovalent cations) within the perovskite structure.

By integrating cesium into the perovskite crystal structure, the resulting triple cation perovskite compositions are more thermally stable and are less sensitive to processing conditions.[35,36] The mixed halide triple cation perovskite solar cells (with both I$^-$ and Br$^-$ as anions) have exhibited higher thermal stability and increased lifetimes under operating conditions. They can also have a high initial stabilized PCE of 21.1%, which reduces to ~18.2% after 250 h of solar illumination under normal working conditions.[36] Such a device can also be further improved by interfacial engineering to retain 95% of the initial efficiency for durations of over 1000 h.[37] High temperature can also lead to the degradation of solar cells, especially those above 85 °C.[38] Such temperatures can lead to solar cell performance degradation due to burn-in, which can lead to chemical changes. Such instability can also be enhanced by exposure to moisture.[39]

The degradation in OIHPs has been observed to occur in three time regimes: an initial period of steep degradation that slows down with time, a period of relatively constant degradation that lasts for the majority of the solar cell's lifetime, and rapid and complete degradation that results in device failure.[40,41] "Burn-in" is the term used to describe the early phase of rapid decline in the stability of PSCs. It is a commercial practice to apply a brief thermal treatment for an acceptable amount of time before delivering electronic devices to customers.[42] This process affects early performance marginally in solar cells. When burn-in time is short in comparison to a device's lifespan, efficiency loss during burn-in is conceptually equivalent to the loss in initial efficiency. The physical process that causes the burn-in, which results in a loss of around 25% of the initial efficiency, remains unknown. However, beyond the solar cell architectures and perovskite formulations, the performance of PSCs also depends on the charge transport layers and electrodes.[14]

Electron Transport Layers (ETLs), Hole Transport Layers (HTLs), and metal electrodes are also critical to PSC stability. In the case of Spiro-OMeTAD hole transporting layers that are widely used in n-i-p PSCs, they undergo crystallization at 80 °C, which degrades their PCE. Furthermore, additives such as the LiTFSI dopant, which are used for the preparation of hole transporting layers, are highly hygroscopic. They can therefore seriously degrade the perovskite layer at low temperatures of 65 °C.[43] Previous work has also shown that during the heating of PSCs to 75 °C for a very extended period (6 h), gold from the top electrode migrates through the Spiro-OMeTAD layer into the perovskite layer. This represents another degradation pathway at higher temperatures.[44] The different ETLs also result in different degradation mechanisms. For example, tin oxide (SnO$_2$) and titanium dioxide (TiO$_2$) are two common ETLs. SnO$_2$ with mismatching ETL/perovskite energy-band levels causes charge accumulation, which leads to solar cell instability at high temperature.[45] A gradual increase in temperature also has a significant effect on crystal structure, phase transition, and the degradation of PSCs. These are associated with decreasing charge carrier diffusion length and the decrease in charge mobility in PSCs.[46] However, despite the remarkable progress that has been made with the development of cesium-based triple cation perovskites, the understanding of the underlying thermally induced degradation phenomena is still very limited. There is, therefore, a need for studies on the degradation mechanisms in cesium-based triple cation perovskites.

Hence, in this study, we explore the temperature-dependent degradation of a triple-cation mixed halide based perovskite active layer (Cs$_{0.05}$ (FA$_{0.95}$MA$_{0.05}$)$_{0.95}$Pb(I$_{0.9}$Br$_{0.05}$)$_3$) in an n-i-p solar cell structure with an FTO/SnO$_2$/perovskite/Spiro-OMeTAD/Au architecture. The study was carried out on unencapsulated devices in an environmental chamber that was used to simulate temperatures of 30–60 °C, which mimic possible operating conditions. The implications of the results are also discussed for the development of PSCs with improved stability.

II. MATERIALS AND METHODS

A. Materials

Fluorine-doped tin oxide (FTO)-coated glass, diisopropoxide bis(acetylacetonate), tin(IV) chloride pentahydrate (SnCl$_4$ 5H$_2$O—98%, Sigma-Aldrich), diluted SnO$_2$ colloidal dispersion (15% in H$_2$O colloidal dispersion, Alfa Aesar), formamidinium iodide (FAI; 98%), methylamine hydrobromide (MABr), cesium iodide (CsI), lead bromide (PbBr$_2$) (99.9%), lead iodide (PbI$_2$; 99.9%), chlorobenzene (anhydrous, 99.8%) dimethyl sulfoxide (DMSO) (anhydrous, 99.9%), dimethylformamide (DMF) (anhydrous, 99.8%), acetone, iso-propyl alcohol (IPA), 4-tert-butylpyridine (tBP), acetonitrile, lithium bis(trifluoromethylsulfonyl) imide (Li-TFSI), 2,2′,7,7′-tetrakis(N,N-di-*p* methoxyphenylamine)-9,9′-spirobifluorene (Spiro-OMeTAD), and anhydrous chlorobenzene were all purchased from Sigma-Aldrich (Natick, MA, USA), while pure gold (99.999%, Lesker) was purchased from Kurt J. Lesker Company (Edward E306A, Easton PA, USA). All the materials were used in their as-received conditions.

B. Device fabrication

The fluorine doped tin oxide (FTO, ~7 Ω sq^{-1}) coated glass substrates were cut into dimensions of 12.5 × 25 mm^2 patterned and

partially etched with zinc powder and 2M hydrochloric acid. The etched substrates were each cleaned for 15 mins in detergent, deionized water, acetone (Sigma-Aldrich), and IPA (Sigma-Aldrich). They were then blow-dried in nitrogen gas, followed by UV–ozone cleaning (Novascan, Main Street Ames, IA, USA) for another 15 mins to remove organic residuals, prior to the deposition of subsequent layers.

An electron transporting layer (ETL) (that comprises SnO_2) was deposited onto FTO-coated glass. The compact SnO_2 deposition was made by dissolving 0.016 g of tin(IV) chloride pentahydrate ($SnCl_4$ $5H_2O$—98%, Sigma-Aldrich) in 1 ml of anhydrous iso-propanol (99.5%, Sigma-Aldrich) before stirring at room temperature (25 °C). The precursor was spin-coated onto the cleaned FTO-coated glass at 2000 rpm for 45 s. This was followed by annealing at 180 °C for 45 min. Subsequently, an additional layer of ETL (nanoparticle SnO_2 layer) from a mixture of diluted SnO_2 colloidal dispersion (15% in H_2O colloidal dispersion, Alfa Aesar) and deionized water in the volume ratio 1:4 was spin coated at 4000 rpm for 45 s. This was then annealed at 150 °C in the air for 30 min.

Subsequently, the normal perovskite absorber stoichiometry of $Cs_{0.05}(FA_{0.95}MA_{0.05})_{0.95}Pb(I_{0.9}Br_{0.05})_3$, typically referred to a triple-cation, was prepared and deposited onto the ETL. The triple cation perovskite precursor was first prepared, following the previous protocol.[47] First, two stock solutions of 0.8M of $FAPbI_3$ and $MAPbBr_3$ perovskite solutions were mixed together in a particular volume ratio. The 0.8M $FAPbI_3$ stock solution was prepared by dissolving 0.481 g FAI (Sigma-Aldrich) and 1.420 g PbI_2 (Sigma-Aldrich) in a 4:1 (v/v) mixture of dimethylformamide (DMF, Sigma-Aldrich) and dimethyl sulfoxide (DMSO, Sigma-Aldrich), which contains an excess of PbI_2. In addition, 0.8M of $MAPbBr_3$ stock solution was prepared by dissolving 0.313 g MABr (Sigma-Aldrich) and 1.130 g $PbBr_2$ (Sigma-Aldrich) in the DMF:DMSO (4:1 volume ratio) solvent, followed by stirring, with excess $PbBr_2$. Then, 40 μl of the 1.5M CsI (Sigma-Aldrich) stock solution (in DMSO solvent) was mixed with 1.5 ml of the previous solution described above. The solution was then spin-coated onto the mesoporous SnO_2 (mp-SnO_2) layer in a two-step process at (i) 2000 for 10 s and (ii) 6000 rpm for 30 s. Chlorobenzene (100 ml) was poured over the spinning substrate 10 s before the completion of the second step to ensure fast crystallization and good film quality. The films were then annealed at 100 °C for 30 min. This was performed inside a glove box in a nitrogen environment.

The hole transport layer (HTL) was deposited using a recently reported recipe.[34] At first, 72 mg of Spiro-OMeTAD was dissolved in 1 ml of chlorobenzene. Later, 35 μl of Li-TFSI solution (260 mg of Li-TFSI dissolved in 1 ml of acetonitrile) and 30 μl of tBP were added to the Spiro-OMeTAD solution and stirred. The mixture was then sonicated for 5 min before spin coating onto the perovskite film at 4000 rpm for 30 s. Finally, a 90 nm thick layer of gold was thermally evaporated onto the Spiro-OMeTAD film at an average deposition rate of 1.1 s^{-1}. This was carried out under high vacuum (pressure of 10^{-6} Torr). A shadow mask was used to achieve the desired device area of 0.1 cm^2.

C. Device characterization

The light absorption behavior of the perovskite films was characterized (in the wavelength range of 200–1100 nm) using an Ultraviolet-Visible (UV–Vis) spectrometer (Avaspec-2048, AVANTES Starline, BV, USA). The morphologies of the perovskite films and cross section element mapping of the PSCs were probed using a Scanning Electron Microscope (SEM) (JEOL JSM-700F, Hollingsworth and Vose, MA, USA) and an Oxford Energy Dispersive Spectroscope (EDS), while the crystallographic characteristics of the perovskite films were determined using an x-ray diffractometer (Malvern PANalytical, Westborough, MA, USA) that was operated at 40 kV and 40 mA under a Cu Kα radiation, with a beta nickel filter.

The current density–voltage measurements (J–V measurements) were obtained using a Keithley source meter unit 2400 system (Keithley, Tektronix, Newark, NJ, USA) that was connected to an Oriel solar simulator (Oriel, Newport Corporation, Irvine, CA, USA). The intensity of light was calibrated at 100 mW/cm^2 using a 91150V silicon reference cell supplied by Newport (MKS/Newport Instruments, Newport Beach, CA, USA). A Weiss environmental chamber (WKL 34, Weiss Umwelttechnik, Reiskirchen-Lindenstruth, Germany) was used to control the temperature in the range of 30 to 60 °C for perovskite solar devices. The exposure parameters from pristine (room temperature) to 60 °C were chosen based on the environmental operating temperatures for solar cells that simulate different environmental conditions with moderate and very high temperatures. Electrochemical Impedance Spectroscopy (EIS) was then used to study the charge transfer characteristics, alongside the J–V measurements within the Weiss environmental. A light gap of 2.24 mm^2 (device area) was used during measurements with a voltage scan between −0.2 and 1.2 V, while the EIS studies were performed using a potentiostat (SP-300, Bio-Logic Instrument, Knoxville, TN, USA) with an AC amplitude of 10 mV in the frequency range between 1 MHz and 10 mHz.

III. RESULTS AND DISCUSSION

A. Microstructure of perovskite film and cross sections of multilayered structure

Scanning Electron Microscopy (SEM) images of the perovskite films are presented in Figs. 1(a)–1(e) for perovskite films exposed to different temperatures for 3 h. Figures 1(a)–1(e) present the SEM images of the perovskite films at different exposed temperatures. The results show that at room-temperature (25 °C), the perovskite layer has equiaxed grain without pinholes. The grain boundaries are also well-defined [Fig. 1(a)], and the average grain size is ~198 ± 9.6 nm.

Figures 1(b) and 1(c) correspond to films exposed to 30 and 40 °C, respectively. The perovskite grain sizes are ~209 ± 7.4 nm (for samples exposed to heat at 30 °C) and ~225 ± 8.1 nm (for samples exposed to heat at 40 °C). The microstructures were also less uniform than those of the room-temperature (25 °C) samples. However, after exposing to heat at 50 and 60 °C for 3 h, a significant difference in microstructural morphology was observed, as shown in Figs. 1(d) and 1(e). The corresponding average grain sizes also reduced to ~248 ± 7.3 and 257 ± 6.7 nm after exposing at 50 and 60 °C, respectively. The region of "high contrast" is attributed to the generation of PbI_2-rich regions in the perovskite films. Similar regions have been reported in prior works on perovskites.[48–50] The film looks rougher as the grain size increases with increasing temperature between pristine (room temperature) and 60 °C.
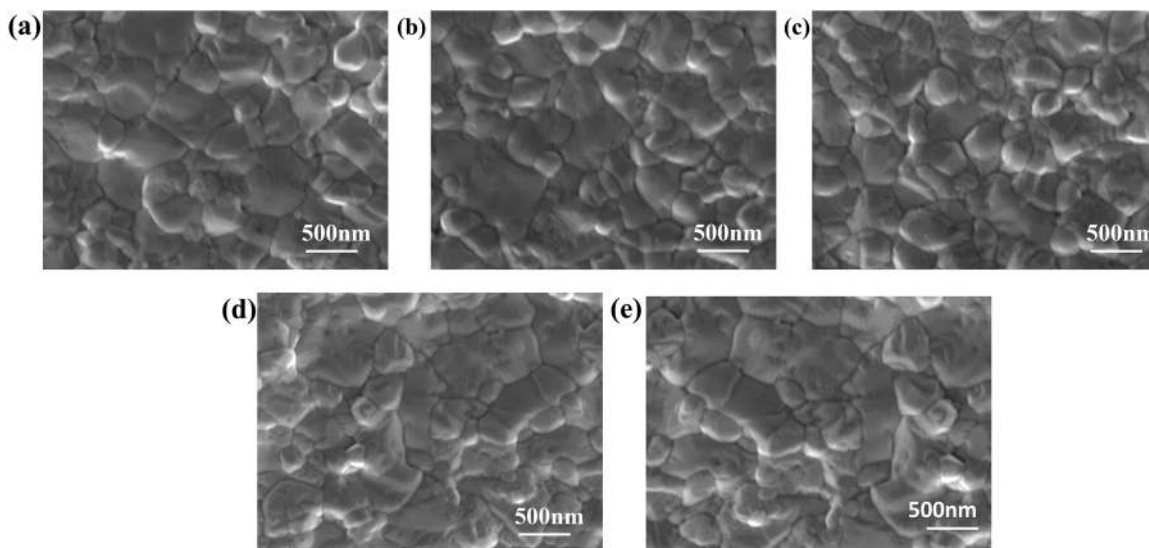
FIG. 1. SEM images of perovskite films before and after exposure to different temperatures for 3 h: (a) pristine, (b) 30 °C, (c) 40 °C, (d) 50 °C, and (e) 60 °C.

We further investigated the interdiffusion of materials across the cross section of the layered PSCs at different exposing temperatures using SEM and Energy Dispersive X-ray Spectroscopy (SEM-EDX). Figures 2(a)–2(e) present the cross-sectional SEM-EDX images that show the diffusion of elements in the device. The results show that Si and Sn are aligned with the layers of glass and FTO/SnO_2, respectively. The perovskite layer is indicated by lead (Pb) and iodine (I) element distribution, while C is from the Spiro-OmeTAD. Before the thermal exposure [Fig. 2(a)], the distributions of I and Pb slightly overlap, and a clear boundary line appears between Pb and Sn, as well as between I and C. Similar images have been reported by Oyewole et al.[34]

In the case of the devices that were exposed to temperatures for 3 h, both I and Pb diffuse toward the SnO_2 layer as the exposure temperature increases [Figs. 2(b)–2(e)]. The diffusion of I is more than that of P, indicating an interpenetration of perovskite diffusion into the SnO_2 layer. We also observed an intermixing of elements within the layered PSC structure [Figs. 2(d) and 2(e)] that can cause interfacial reactions. The interfacial reactions can lead to interfacial defects, which can affect transportation of charges. Recombination can also take place at the sites of the defects, which can reduce the performance characteristics of the PSCs.

B. Structure and optical properties

To understand the structure and optical behavior of the films under exposed temperature, we analyzed the films using x-ray diffractometry (XRD) and UV–vis spectroscopy. Figure 4(a) presents XRD patterns of perovskite films exposed at 30, 40, 50, and 60 °C. The films exhibited diffraction peaks at 2θ angles of 14.01°, 19.86°, 24.35°, 28.19°, 31.65°, 34.78°, 40.31°, and 42.87°. These correspond, respectively, to the (101), (012), (021), (202), (211), (122), (024), and (131) planes and the formation of the black (alpha) perovskite phase.[51] The above-mentioned results show that all the films corresponded to the α perovskite phase, with some trace amounts of segregated PbI_2. The peak at 12.7° can also be assigned to be the (001) plane of the PbI_2 hexagonal structure.[52] The remaining peaks corresponded to the FTO substrate. However, we also observed that the (101) perovskite peaks had the highest intensities in all of the samples. This suggests that nucleation and growth of the perovskite crystals were traced in (101) planes.

However, as the exposing temperature increased, the peak intensities decreased [Fig. 3(a)]. It is also interesting to note here that the (001) peak corresponds to the presence of PbI_2,[13] which is clearly present at 60 °C. This suggests that the thermal decomposition of perovskites (into PbI_2) occurs with increasing temperature.[15] Finally, it is important to note that the intensity of the main peak (101) decreases with increasing exposure temperature [Fig. 3(a)]. This is consistent with the above-mentioned observation of the formation of PbI_2 with increasing exposure temperature. Thus, the volume fraction of perovskites should reduce as the incidence of PbI_2 increases.

C. Optical absorption spectra

The optical absorption spectra of the perovskite films are presented in Fig. 3(b) for films that were exposed for 3 h at temperatures between 30 and 60 °C. The shapes of the spectra are largely unaffected for wavelengths between 500 and 850 nm wavelength, indicating that the bandgaps of the perovskite films were mostly unaffected by exposing in this temperature regime. However, the absorption intensity reduced significantly with increasing exposing temperature [Fig. 3(b)]. Hence, the exposure temperature of the film will influence optical absorption as the intensity of absorption is closely related to the photogeneration process. This is consistent with the trends in the normalized absorbance data present in Fig. 3(b).
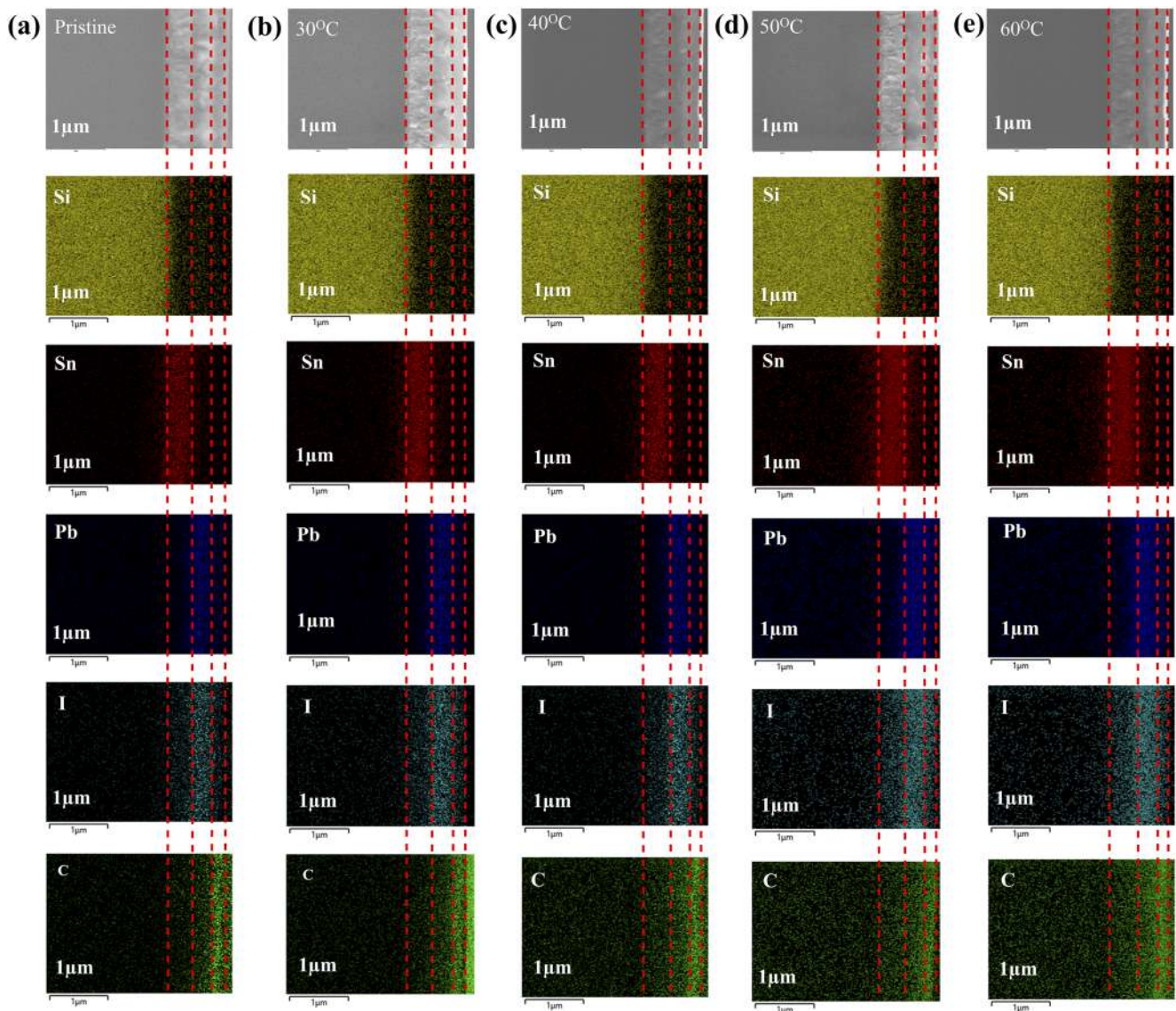
FIG. 2. Cross-sectional SEM image and corresponding EDX elemental mapping of multilayers (Si, Sn, Pb, I, and C): (a) pristine, (b) 30 °C, (c) 40 °C, (d) 50 °C, and (e) 60 °C for 3 h.

D. Solar cell device performance characteristics

The current density–voltage (J–V) curves and the solar cell/device performance parameters obtained in forward and reverse bias conditions under 1 sun illumination (AM 1.5 G) are presented in Fig. 5(a) for the as-fabricated device. The overall best performing device yields a photocurrent density (J_{SC}) of 22.76 ± 0.51 mA/cm^2, an open circuit potential (V_{OC}) of 1.06 ± 0.02 V, a fill factor (FF) of 80.1 ± 1.87%, and a photoconversion efficiency of 19.3 ± 0.86%.

J–V curves obtained from solar cells that were exposed to temperatures between 30 and 60 °C for durations of 0, 0.5, 1, 2, and 3 h (180 min) are presented in Figs. 4(b)–4(e). In the case of the devices

being operated at 30 °C, the J–V curves and the device performance characteristics are presented in Fig. 4(b) for the forward and reverse scans. The J–V curves obtained from the forward and reverse scans yield V_{OC} and J_{SC} values of (1.03 ± 0.03 V and 20.21 ± 1.07 mA/cm^2) and (1.05 ± 0.01 V and 21.31 ± 1.06 mA/cm^2), respectively. However, after 3 h of operation, the corresponding values of V_{OC} and J_{SC} obtained from the forward and reverse scan are reduced to (0.92 ± 0.03 V and 17.23 ± 1.20 mA/cm^2) and (0.95 ± 0.02 V and 17.77 ± 1.09 mA/cm^2), respectively. Meanwhile, the device performance in Fig. 4(c) corresponds to forward and reverse scan results of (1.02 ± 0.01 V and 21.50 ± 0.86 mA/cm^2) and (1.03 ± 0.01 V and
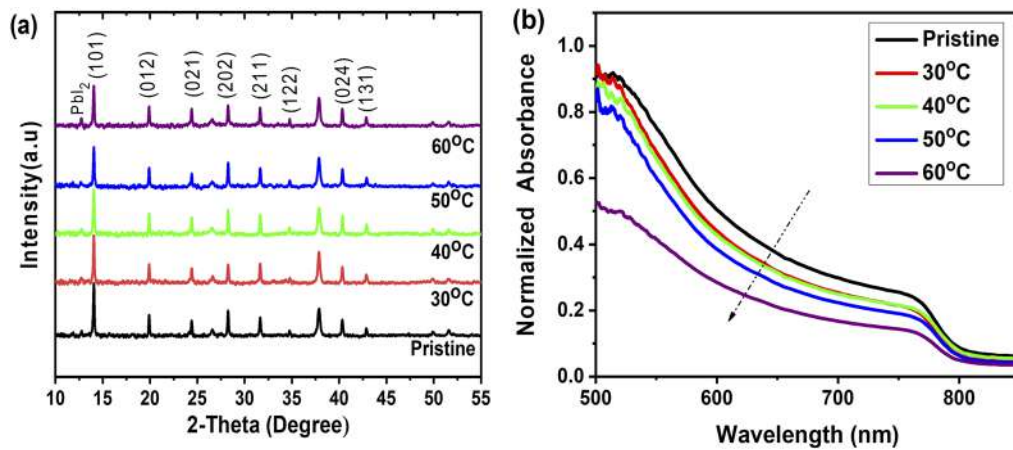
FIG. 3. (a) XRD patterns. (b) Normalized UV–vis absorption spectra exposed to different temperatures.

21.54 ± 0.73 mA/cm^2), respectively, at 40 °C for 0 h. After 3 h of operation at 40 °C, V_{OC} and J_{SC} dropped to (0.87 ± 0.02 V and 17.41 ± 0.82 mA/cm^2) for the forward scan and (0.94 ± 0.02 V and 17.61 ± 0.75 mA/cm^2) for the reverse scan. Furthermore, the hysteresis between the forward and reverse scans was minimal at 0 h, in contrast with the hysteresis observed after 3 h of operation.

Similar trends in the hysteresis curves have been reported for PSCs.[53] These are typically attributed to the effects of defects in the perovskite absorbers of the solar cell structures.[53] The hysteresis loop

has also been linked to the ion migration or accumulation phenomena. This effect is also suggested for our devices as charge accumulation in the device increases over time with increasing operating temperature. Table S1 presents the summary of device parameters for all the devices that were exposed to different temperatures. The current density decreases with increasing operating temperature of the PSCs. The current density decreased rapidly in comparison to the open-circuit voltage in the J–V curves. At this stage, burn-in decay was most noticeable, especially under short-circuit conditions.
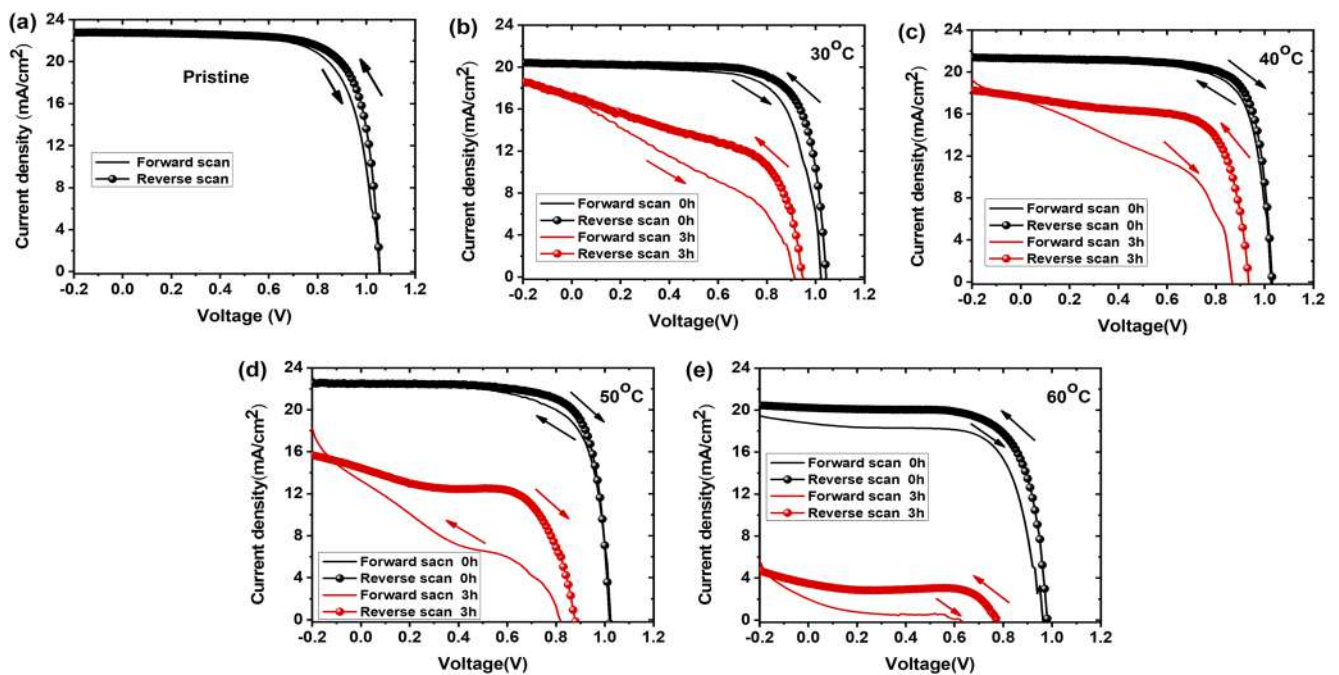

FIG. 4. J–V characteristics of (a) as-fabricated device in forward and reverse scan directions, (b) 30 °C, (c) 40 °C, (d) 50 °C, and (e) 60 °C for 0 and 3 h.

The trends in the solar cell performance characteristics are summarized in Table S1. These generally decrease with increasing exposure duration and are particularly evident after exposure at 50 and 60 °C. In the case of the solar cells being exposed at 50 °C for up to 3 h, the forward scan values of V_{OC} and J_{SC} were (1.02 ± 0.03 V and 22.36 ± 0.75 mA/cm^2), while the reverse scan values were (1.02 ± 0.03 V and 22.56 ± 0.52 mA/cm^2) for 0 h. The recorded values after 3 h were (0.82 ± 0.03 V, 13.26 ± 1.14 mA/cm^2) and (0.88 ± 0.03 V and 14.45 ± 0.85 mA/cm^2) for forward and reverse scans, respectively. The differences between the degradation rates at V_{OC} and J_{SC} are attributed to the differences in the accumulation of charge carriers and internal electric fields, as in prior work.[54] This suggests a strong dependence of temperature-induced degradation on actual operation conditions.

In the case of an operating temperature of 60 °C [Fig. 4(e)], the forward and reverse scan (V_{OC} and J_{SC}) values obtained for 0 h are (0.97 ± 0.03 V and 18.76 ± 1.93 mA/cm^2) and (0.99 ± 0.02 V and 20.23 ± 1.15 mA/cm^2), respectively. A dramatic degradation in the parameters is observed after 3 h of operation, with values of V_{OC} and J_{SC} of (0.63 ± 0.02 V and 2.99 ± 0.93 mA/cm^2) for the forward scan and (0.78 ± 0.02 V and 4.22 ± 0.77 mA/cm^2) for the reverse scan. Therefore, regardless of lighting conditions, the values of V_{OC} and J_{SC} gradually reduce with both temperature and exposure duration (Figs. S1 and S2).

Furthermore, beyond the hysteresis effects at operating temperatures of 50 and 60 °C, we also noticed an S-shaped kink in the J–V curve in the PSCs after 3 h [Figs. 4(d) and 4(e)]. This was not observed in devices operated at 30 and 40 °C. The S-shaped kink is attributed to poor charge extraction at the interfaces. This may result ultimately in unfavorable temperature effects[55] that are associated with charge build-up across the interfaces between the perovskite and the ETL ~ or HTL.

The solar cell's performance characteristics obtained from the J–V reverse scans are also presented in Figs. 5(a)–5(d) in normalized J_{SC}, V_{OC}, FF, and PCE during thermal aging of the devices. Each result shows the temperature operation ranging from 30 to 60 °C. Note that the devices exposed to 60 °C for 3 h exhibited drastic degradation under these conditions. However, the V_{OC} and FF at 60 °C were reduced to 77.2% and 71.1% of their initial values after 3 h, respectively [Figs. 5(a) and 5(c)]. The overall device J_{SC} exhibits a significant reduction compared to V_{OC} and FF, which deteriorated to 17.6% of the initial value after the completion of 3 h operation [Fig. 5(b)]. Consequently, the resulting PCE dropped rapidly to 12.1% of the initial value during 60 °C thermal stress for 3 h [Fig. 5(d)].

In an effort to better understand the evolution of short-circuit current (J_{SC}) with an increasing temperature effect, plots of current density vs time are presented in Figs. 6(a)–6(d). Note that the degradation in current density vs time is initially characterized by linear degradation. This is then followed by an exponential decay regime [Figs. 6(a) and 6(b)]. Within 3 h of operation at 30 °C, J_{SC} drops to 86% of its initial value (20.31–17.18 mA/cm^2). Similarly, in the case of 50 and 60 °C [Figs. 6(c) and 6(d)], we noticed a fast or rapid exponential degradation regime, frequently followed by a linear degradation, in which performance decreases steadily. This suggests that the decay dynamics of the initial component are higher,
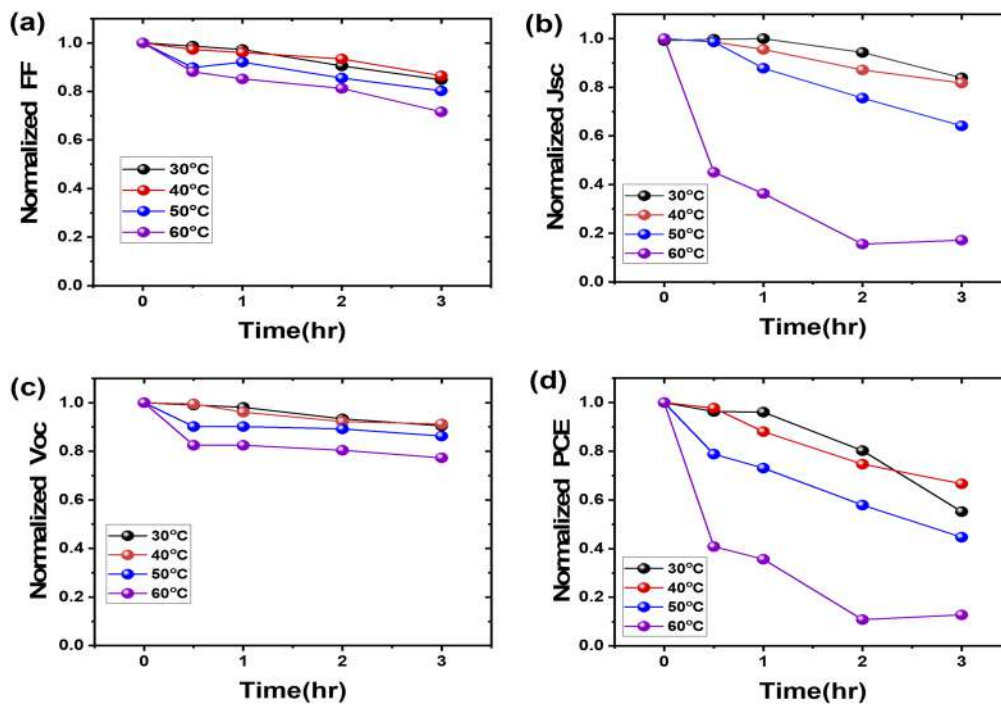

FIG. 5. Variation in normalized photovoltaic parameters extracted from the I–V curves at different temperatures: (a) V_{OC}, (b) J_{SC}, (c) FF, and (d) PCE with time.
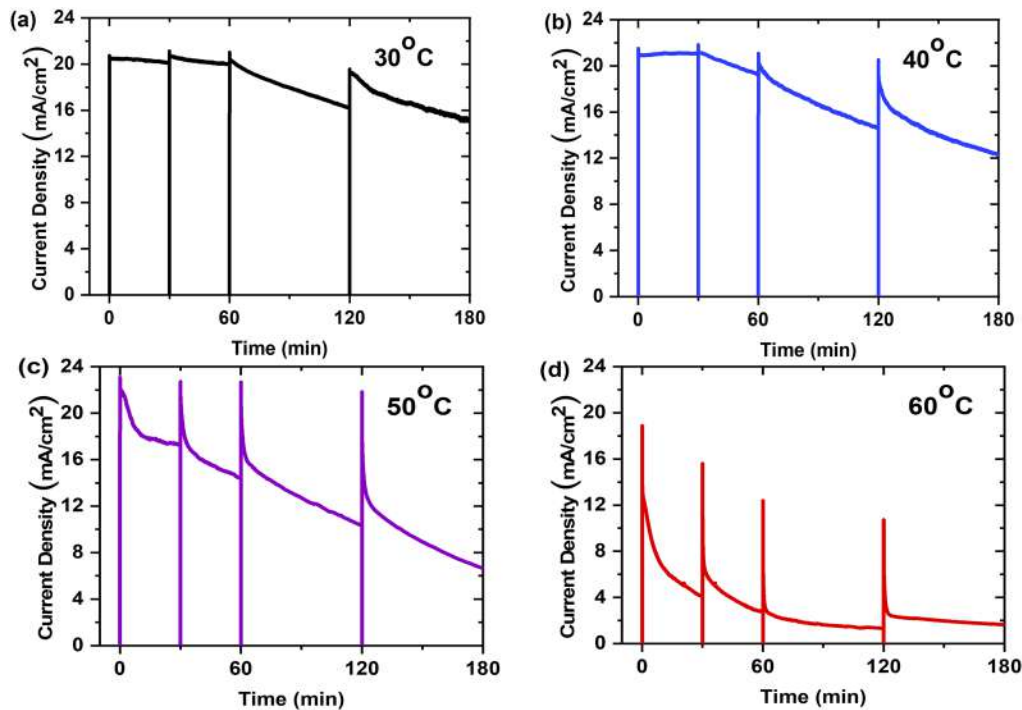
FIG. 6. Temperature-dependence of photocurrent density (J_{SC}) vs time (min) for PSCs at different exposed temperatures: (a) 30 °C, (b) 40 °C, (c) 50 °C, and (d) 60 °C. J_{SC} was measured at 0, 30, 60, 120, and 180 min.

and the subsequent linear loss is limited as temperature increases up to 50 °C.

In contrast, at elevated temperature (60 °C), the sharp decline in short circuit current degradation is very rapid, and the initial period of fast degradation is characterized as burn-in decay.[40,41] A burn-in loss of up to 17.1% was observed in the initial value (20.23–3.47 mA/cm^2) after a time span of 3 h. The drop in the short circuit current density corresponds to the primary result

that was obtained from the J–V curves [Figs. 4(a)–4(d)]. We also attribute the reduction in J_{SC} (as the temperature increases) to exciton trapping that occurs at the interface between the SnO$_2$/perovskite layers where the occurrence of the delamination prevents the splitting of excitons and the collection of charge carriers. It is important to note here that the occurrence of burn-in has also been suggested to be dependent on contact–layer interfaces.[40]
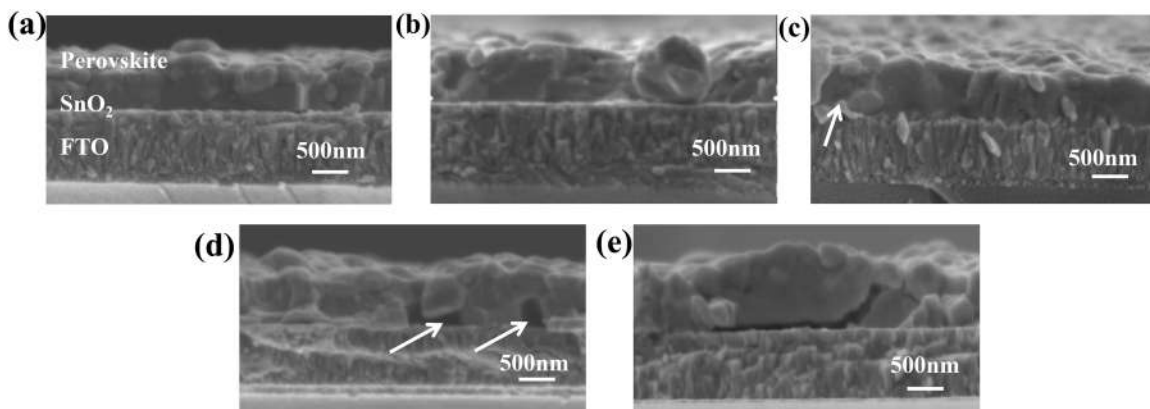

FIG. 7. SEM cross-sectional images of FTO/SnO2/perovskite at different exposure temperatures for 3 h: (a) pristine, (b) 30 °C, (c) 40 °C, (d) 50 °C, and (e) 60 °C.

E. The role of interfaces in the thermally induced degradation of PSCs

In an effort to understand the thermally induced decomposition that occurs across the layers of devices, SEM was used to characterize cross-sectional views of the layers and their interfaces. This was carried out before and after exposure to temperature for half-device configurations of $FTO/SnO_2/(Cs_{0.05}(FA_{0.95}MA_{0.05})_{0.95}Pb(I_{0.9}Br_{0.05})_3)$. Figures 7(a)–7(e) show the cross-sectional SEM images of half devices for the pristine and degraded layers exposed for 3 h. In the pristine case, the stacked multilayers exhibit uniform microstructures with no evidence of microvoids or cracks at the interface between the layers [Fig. 7(a)]. Similar microstructures were also observed in the cross sections of the device that were exposed to 30 °C [Fig. 7(b)].

However, as the temperatures increase from 30 to 40/50 °C, evidence of microvoids was observed along the interfaces [Figs. 7(c) and 7(d)]. The microvoids coalesced to form bigger cracks, as the size of the grain increases. Evidence of interfacial cracks [Figs. 7(d) and 7(e)] was also observed in the samples that were exposed at 50 and 60 °C. The occurrence of interfacial cracks is attributed to the thermal stress that is induced due to the thermal expansion mismatch between the layers in the PSCs. Such mismatch stresses can

also be amplified by the crack-tip fields associated with the presence of interfacial cracks[56] that can give rise to crack driving forces that are sufficient to grow the interfacial cracks in ways that may lead to the delamination of the perovskite films during exposure at 60 °C [Fig. 7(e)]. Therefore, the delamination of the perovskite films may be the one to restrict charge transfer between the perovskite and the SnO_2 layer, resulting in a decrease in PSCs during operation [see Figs. 8(c) and 8(d)].

In an effort to relate the occurrence of interfacial microvoids and crack occurrence of interfacial microvoids to charge transport and recombination processes in PSCs, Electrochemical Impedance Spectroscopy (EIS) was carried out to characterize the devices exposed to different exposure temperatures over time. Nyquist plots obtained as a function of temperature and time are shown in Figs. 8(a)–8(d). Two semi-circular features that are typical for any PSC device with two relaxation processes are clearly observed in the Nyquist plots. The semi-circle in the high frequency region is attributed to the charge transport resistance (R_{tr}) of the device, while the one in the low-frequency regime corresponds to the recombination resistance (R_{rec}) of the device.[57] With the evolution of V_{OC}, it is expected that the decrease in R_{rec} should be more severe with temperature. However, an increase in R_{rec} over time indicates a
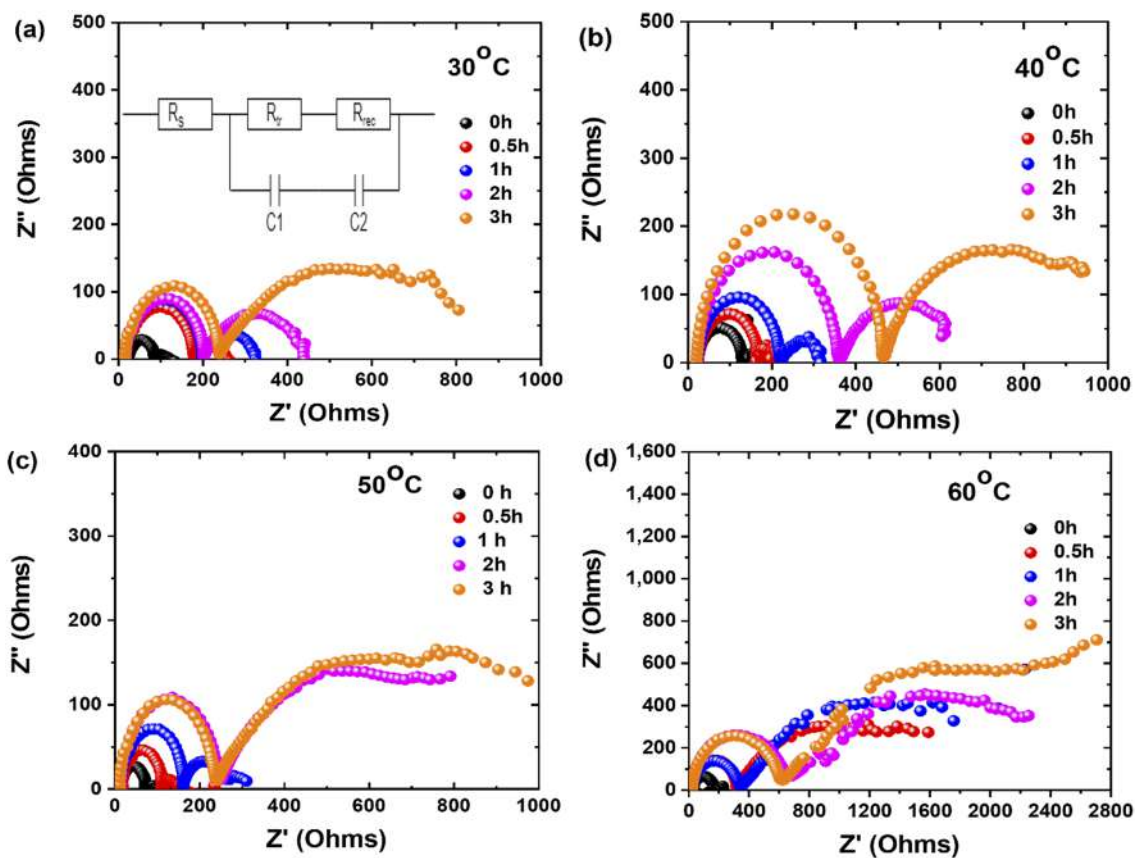

FIG. 8. Nyquist plot of PSCs obtained at open-circuit voltage under light: (a) 30 °C, (b) 40 °C, (c) 50 °C, and (d) 60 °C at 0, 0.5, 1, 2, and 3 h.
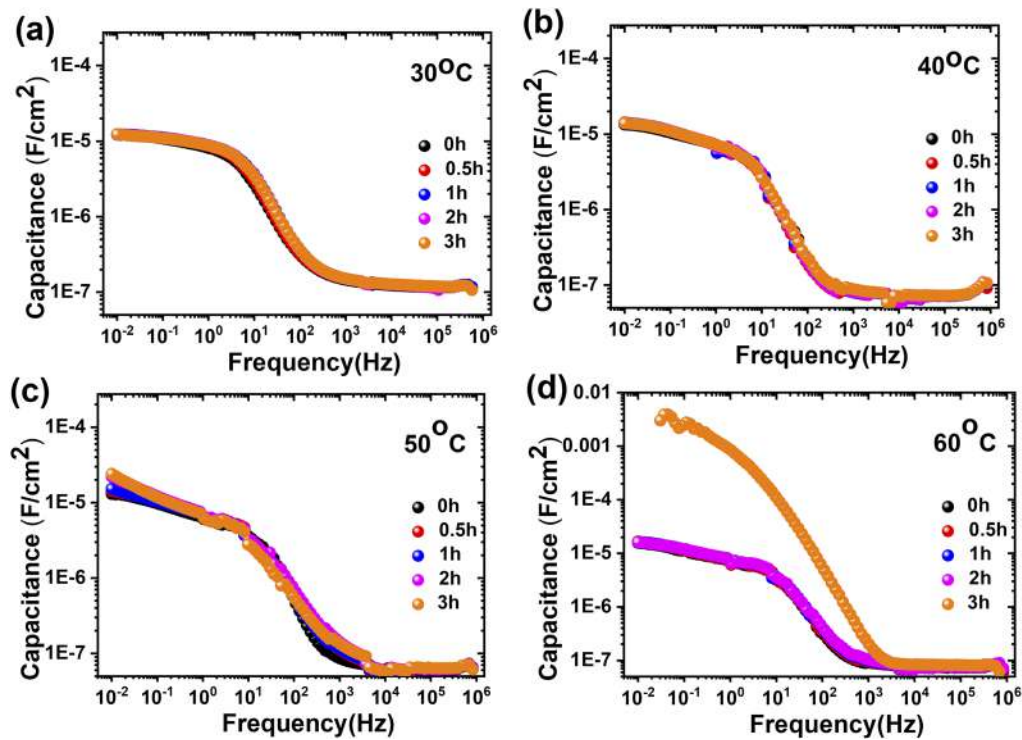
FIG. 9. Capacitance per unit area vs frequency under dark at different temperatures: (a) 30 °C, (b) 40 °C, (c) 50 °C, and (d) 60 °C.

degradation of the device charge transport properties. After fitting the impedance spectra to an equivalent circuit shown in the inset of Fig. 8(a), we extracted R_{tr} values for the PSCs exposed to different temperatures for different durations. The results are summarized in Table S2. Note that the values of R_{tr} were found to increase with thermal exposure time for each of the temperatures that was considered in this study.

For the device operating temperature of 30 °C, R_{tr} increased from a value of 62.43 ± 0.82 to 222.43 ± 0.74 Ω while for the temperature of 60 °C, it increased from 126.47 ± 0.44 to 663.26 ± 0.51 Ω. The increase in R_{tr} is a clear indication that the charge extraction and transport phenomena in the PSC devices decreased with increasing temperature. Since poor charge transport in PSCs can also lead to ionic or electronic charge accumulation at the interfaces, we also explored the increase in capacitance that occurs with increasing exposure temperatures, as shown in the capacitance–frequency (CF) plots in Figs. 9(a)–9(d).

CF plots obtained from the EIS studies that were performed in the light are presented in Figs. 9(a)–9(d). In the CF plots, the capacitance spectral signature is in two steps: the low frequency indicates the ionic and electronic behavior of the perovskite surface, while the dipole polarization[58,59] is noted for the intermediate frequency. During the operating temperature, we clearly see an increase in the capacitance in the low frequency region with high exposure temperature (60 °C) with time. This is attributed to the piling-up of electronic charges at the interfaces as a result of higher charge transport resistance [see Fig. 8(d)] or poor charge transport across

the interfaces between the perovskite and the SnO_2 layer. This is consistent with the increased incidence of microvoids and interfacial cracks/delamination that was observed in the devices exposed at 60 °C, as shown in Fig. 7(e).

IV. CONCLUSION

This paper presents the results of a study of the effects of temperature on the performance of PSCs. The results show clearly that increasing the operating temperature enhances the formation of microvoids and interfacial cracks between the perovskite layer and the ETL. These defects degrade device performance along with the effects of burn-in at higher temperatures (50–60 °C). The impedance spectroscopy analysis revealed an increase in charge transfer resistance due to ionic contributions at the perovskite/SnO_2 interface. The capacitance measurement also revealed that the piling up of charges during the degradation of PSCs is associated with the presence of defects that evolve with increasing service exposure to temperature and light.

SUPPLEMENTARY MATERIAL

The supplementary material contains the summary of device parameters of PSCs at different operating temperatures for 3 h, the summary of the impedance spectroscopic parameter of PSCs extracted from the Nyquist plot, and the intermittent J–V curve for both forward and reverse scans at different temperatures and times.

ACKNOWLEDGMENTS

AUTHOR DECLARATIONS

Conflict of Interest

The authors have no known competing financial interests.

DATA AVAILABILITY

The data that support the findings of this study are available from the corresponding author upon reasonable request.

REFERENCES

[1] M. Green, E. Dunlop, J. Hohl-Ebinger, M. Yoshita, N. Kopidakis, and X. Hao, "Solar cell efficiency tables (version 57)," Prog. Photovoltaics Res. Appl. **29**, 3–15 (2021).

[2] A. Kojima, K. Teshima, Y. Shirai, and T. Miyasaka, "Organometal halide perovskites as visible-light sensitizers for photovoltaic cells," J. Am. Chem. Soc. **131**, 6050–6051 (2009).

[3] S. Sun, T. Salim, N. Mathews, M. Duchamp, C. Boothroyd, G. Xing, T. C. Sum, and Y. M. Lam, "The origin of high efficiency in low-temperature solution-processable bilayer organometal halide hybrid solar cells," Energy Environ. Sci. **7**, 399–407 (2014).

[4] N. K. Tailor, M. Abdi-Jalebi, V. Gupta, H. Hu, M. I. Dar, G. Li, and S. Satapathi, "Recent progress in morphology optimization in perovskite solar cell," J. Mater. Chem. A **8**, 21356–21386 (2020).

[5] H. J. Snaith, "Perovskites: The emergence of a new era for low-cost, high-efficiency solar cells," J. Phys. Chem. Lett. **4**, 3623–3630 (2013).

[6] W. S. Yang, J. H. Noh, N. J. Jeon, Y. C. Kim, S. Ryu, J. Seo, and S. I. Seok, "High-performance photovoltaic perovskite layers fabricated through intramolecular exchange," Science **348**, 1234–1237 (2015).

[7] W. S. Yang, B.-W. Park, E. H. Jung, N. J. Jeon, Y. C. Kim, D. U. Lee, S. S. Shin, J. Seo, E. K. Kim, J. H. Noh, and S. I. Seok, "Iodide management in formamidinium-lead-halide-based perovskite layers for efficient solar cells," Science **356**, 1376–1379 (2017).

[8] Q. Jiang, Y. Zhao, X. Zhang, X. Yang, Y. Chen, Z. Chu, Q. Ye, X. Li, Z. Yin, and J. You, "Surface passivation of perovskite film for efficient solar cells," Nat. Photonics **13**, 460–466 (2019).

[9] H. Min, M. Kim, S.-U. Lee, H. Kim, G. Kim, K. Choi, J. H. Lee, and S. I. Seok, "Efficient, stable solar cells by using inherent bandgap of α-phase formamidinium lead iodide," Science **366**, 749–753 (2019).

[10] S. Arya, P. Mahajan, R. Gupta, R. Srivastava, N. k. Tailor, S. Satapathi, R. R. Sumathi, R. Datt, and V. Gupta, "A comprehensive review on synthesis and applications of single crystal perovskite halides," Prog. Solid State Chem. **60**, 100286 (2020).

[11] M. Stolterfoht, P. Grischek, P. Caprioglio, C. M. Wolff, E. Gutierrez-Partida, F. Peña-Camargo, D. Rothhardt, S. Zhang, M. Raoufi, J. Wolansky, M. Abdi-Jalebi, S. D. Stranks, S. Albrecht, T. Kirchartz, and D. Neher, "How to quantify the efficiency potential of neat perovskite films: Perovskite semiconductors with an implied efficiency exceeding 28%," Adv. Mater. **32**, e2000080 (2020).

[12] M. A. Green, A. Ho-Baillie, and H. J. Snaith, "The emergence of perovskite solar cells," Nat. Photonics **8**, 506–514 (2014).

[13] J. Yang, X. Liu, Y. Zhang, X. Zheng, X. He, H. Wang, F. Yue, S. Braun, J. Chen, J. Xu, Y. Li, Y. Jin, J. Tang, C. Duan, M. Fahlman, and Q. Bao, "Comprehensive understanding of heat-induced degradation of triple-cation mixed halide perovskite for a robust solar cell," Nano Energy **54**, 218–226 (2018).

[14] C. C. Boyd, R. Cheacharoen, T. Leijtens, and M. D. McGehee, "Understanding degradation mechanisms and improving stability of perovskite photovoltaics," Chem. Rev. **119**, 3418–3451 (2019).

[15] J. Torres, J. Sanchez-Diaz, J. M. Rivas, J. de la Torre, I. Zarazua, and D. Esparza, "Electrical properties and J-V modeling of perovskite (CH$_3$NH$_3$PbI$_3$) solar cells after external thermal exposure," Sol. Energy **222**, 95–102 (2021).

[16] R. K. Misra, S. Aharon, B. Li, D. Mogilyansky, I. Visoly-Fisher, L. Etgar, and E. A. Katz, "Temperature- and component-dependent degradation of perovskite photovoltaic materials under concentrated sunlight," J. Phys. Chem. Lett. **6**, 326–330 (2015).

[17] J. A. Schwenzer, T. Hellmann, B. A. Nejand, H. Hu, T. Abzieher, F. Schackmar, I. M. Hossain, P. Fassl, T. Mayer, W. Jaegermann, U. Lemmer, and U. W. Paetzold, "Thermal stability and cation composition of hybrid organic-inorganic perovskites," ACS Appl. Mater. Interfaces **13**, 15292–15304 (2021).

[18] E. J. Juarez-Perez, Z. Hawash, S. R. Raga, L. K. Ono, and Y. Qi, "Thermal degradation of CH$_3$NH$_3$PbI$_3$ perovskite into NH$_3$ and CH$_3$I gases observed by coupled thermogravimetry-mass spectrometry analysis," Energy Environ. Sci. **9**, 3406–3410 (2016).

[19] W. Huang, S. Sadhu, and S. Ptasinska, "Heat- and gas-induced transformation in CH$_3$NH$_3$PbI$_3$ perovskites and its effect on the efficiency of solar cells," Chem. Mater. **29**, 8478–8485 (2017).

[20] N. Aristidou, I. Sanchez-Molina, T. Chotchuangchutchaval, M. Brown, L. Martinez, T. Rath, and S. A. Haque, "The role of oxygen in the degradation of methylammonium lead trihalide perovskite photoactive layers," Angew. Chem., Int. Ed. **54**, 8208–8212 (2015).

[21] Y. Li, X. Xu, C. Wang, B. Ecker, J. Yang, J. Huang, and Y. Gao, "Light-induced degradation of CH$_3$NH$_3$PbI$_3$ hybrid perovskite thin film," J. Phys. Chem. C **121**, 3904–3910 (2017).

[22] M. Liu, M. B. Johnston, and H. J. Snaith, "Efficient planar heterojunction perovskite solar cells by vapour deposition," Nature **501**, 395–398 (2013).

[23] T. A. Berhe, W.-N. Su, C.-H. Chen, C.-J. Pan, J.-H. Cheng, H.-M. Chen, M.-C. Tsai, L.-Y. Chen, A. A. Dubale, and B.-J. Hwang, "Organometal halide perovskite solar cells: Degradation and stability," Energy Environ. Sci. **9**, 323–356 (2016).

[24] T. T. Ava, A. Al Mamun, S. Marsillac, and G. Namkoong, "A review: Thermal stability of methylammonium lead halide based perovskite solar cells," Appl. Sci. **9**, 188 (2019).

[25] Q. Fu, X. Tang, B. Huang, T. Hu, L. Tan, L. Chen, and Y. Chen, "Recent progress on the long-term stability of perovskite solar cells," Adv. Sci. **5**, 1700387 (2018).

[26] O. A. Syzgantseva, M. Saliba, M. Grätzel, and U. Rothlisberger, "Stabilization of the perovskite phase of formamidinium lead triiodide by methylammonium, Cs, and/or Rb doping," J. Phys. Chem. Lett. **8**, 1191–1196 (2017).

[27] C. M. Sutter-Fella, Y. Li, M. Amani, J. W. Ager, F. M. Toma, E. Yablonovitch, I. D. Sharp, and A. Javey, "High photoluminescence quantum yield in band gap tunable bromide containing mixed halide perovskites," Nano Lett. **16**, 800–806 (2016).

[28] R. K. Koech, R. Ichwani, J. L. Martin, D. O. Oyewole, O. V. Oyelade, Y. A. Olanrewaju, D. M. Sanni, S. A. Adeniji, R. L. Grimm, A. Bello, O. K. Oyewole, E. Ntsoenzok, and W. O. Soboyejo, "A study of the effects of a thermally evaporated nanoscale CsBr layer on the optoelectronic properties and stability of formamidinium-rich perovskite solar cells A study of the effects of a thermally evaporated nanoscale CsBr layer on the optoelectronic," AIP Adv. **11**, 095112 (2021).

[29] R. Cheacharoen, C. C. Boyd, G. F. Burkhard, T. Leijtens, J. A. Raiford, K. A. Bush, S. F. Bent, and M. D. McGehee, "Encapsulating perovskite solar cells to withstand damp heat and thermal cycling," Sustainable Energy Fuels **2**, 2398–2406 (2018).

[30] D. P. McMeekin, G. Sadoughi, W. Rehman, G. E. Eperon, M. Saliba, M. T. Hörantner, A. Haghighirad, N. Sakai, L. Korte, B. Rech, M. B. Johnston, L. M. Herz, and H. J. Snaith, "A mixed-cation lead mixed-halide perovskite absorber for tandem solar cells," Science **351**, 151–155 (2016).

[31] C. A. Aranda, L. Caliò, and M. Salado, "Toward commercialization of stable devices: An overview on encapsulation of hybrid organic-inorganic perovskite solar cells," Crystals **11**, 519 (2021).

[32] B. Brunetti, C. Cavallo, A. Ciccioli, G. Gigli, and A. Latini, "On the thermal and thermodynamic (in)stability of methylammonium lead halide perovskites," Sci. Rep. **6**, 31896 (2016).

[33]B. Salhi, Y. S. Wudil, M. K. Hossain, A. Al-Ahmed, and F. A. Al-Sulaiman, "Review of recent developments and persistent challenges in stability of perovskite solar cells," Renewable Sustainable Energy Rev. **90**, 210–222 (2018).

[34]D. O. Oyewole, R. K. Koech, R. Ichwani, R. Ahmed, J. Hinostroza Tamayo, S. A. Adeniji, J. Cromwell, E. Colin Ulloa, O. K. Oyewole, B. Agyei-Tuffour, L. V. Titova, N. A. Burnham, and W. O. Soboyejo, "Annealing effects on interdiffusion in layered FA-rich perovskite solar cells," AIP Adv. **11**, 065327 (2021).

[35]W. Tan, A. R. Bowing, A. C. Meng, M. D. McGehee, and P. C. Mclntyre, "Thermal stability of mixed cation metal halide perovskites in air," ACS Appl. Mater. Interfaces **10**(6), 5485–5491 (2018).

[36]M. Saliba, T. Matsui, J.-Y. Seo, K. Domanski, J.-P. Correa-Baena, M. K. Nazeeruddin, S. M. Zakeeruddin, W. Tress, A. Abate, A. Hagfeldt, and M. Grätzel, "Cesium-containing triple cation perovskite solar cells: Improved stability, reproducibility and high efficiency," Energy Environ. Sci. **9**, 1989–1997 (2016).

[37]J. A. Christians, P. Schulz, J. S. Tinkham, T. H. Schloemer, S. P. Harvey, B. J. Tremolet de Villers, A. Sellinger, J. J. Berry, and J. M. Luther, "Tailored interfaces of unencapsulated perovskite solar cells for >1,000 hour operational stability," Nat. Energy **3**, 68 (2018).

[38]T. Matsui, T. Yamamoto, T. Nishihara, R. Morisawa, T. Yokoyama, T. Sekiguchi, and T. Negami, "Compositional engineering for thermally stable, highly efficient perovskite solar cells exceeding 20% power conversion efficiency with 85 °C/85% 1000 h stability," Adv. Mater. **31**, e1806823 (2019).

[39]G. Divitini, S. Cacovich, F. Matteocci, L. Cinà, A. Di Carlo, and C. Ducati, "*In situ* observation of heat-induced degradation of perovskite solar cells," Nat. Energy **1**, 15012 (2016).

[40]W. R. Mateker and M. D. McGehee, "Progress in understanding degradation mechanisms and improving stability in organic photovoltaics," Adv. Mater. **29**, 1603940 (2017).

[41]C. H. Peters, I. T. Sachs-Quintana, W. R. Mateker, T. Heumueller, J. Rivnay, R. Noriega, Z. M. Beiley, E. T. Hoke, A. Salleo, and M. D. McGehee, "The mechanism of burn-in loss in a high efficiency polymer solar cell," Adv. Mater. **24**, 663–668 (2012).

[42]P.-H. Lee, C.-C. Torng, and Y.-C. Lin, "Determination of the optimal accelerated burn-in time under Arrhenius–Lognormal distribution assumption," Appl. Math. Model. **35**, 4023–4030 (2011).

[43]C. D. Bailie, E. L. Unger, S. M. Zakeeruddin, M. Grätzel, and M. D. McGehee, "Melt-infiltration of spiro-OMeTAD and thermal instability of solid-state dye-sensitized solar cells," Phys. Chem. Chem. Phys. **16**, 4864–4870 (2014).

[44]A. K. Jena, M. Ikegami, and T. Miyasaka, "Severe morphological deformation of spiro-OMeTAD in $(CH_3NH_3)PbI_3$ solar cells at high temperature," ACS Energy Lett. **2**, 1760–1761 (2017).

[45]L. Xiong, Y. Guo, J. Wen, H. Liu, G. Yang, P. Qin, and G. Fang, "Review on the application of SnO_2 in perovskite solar cells," Adv. Funct. Mater. **28**, 1802757 (2018).

[46]R. L. Milot, G. E. Eperon, H. J. Snaith, M. B. Johnston, and L. M. Herz, "Temperature-dependent charge-carrier dynamics in $CH_3NH_3PbI_3$ perovskite thin films," Adv. Funct. Mater. **25**, 6218–6227 (2015).

[47]E. Gutierrez-Partida, H. Hempel, S. Caicedo-Dávila, M. Raoufi, F. Peña-Camargo, M. Grischek, R. Gunder, J. Diekmann, P. Caprioglio, K. O. Brinkmann, H. Köbler, S. Albrecht, T. Riedl, A. Abate, D. Abou-Ras, T. Unold, D. Neher, and M. Stolterfoht, "Large-grain double cation perovskites with 18 μs lifetime and high luminescence yield for efficient inverted perovskite solar cells," ACS Energy Lett. **6**, 1045–1054 (2021).

[48]J. Chang, H. Zhu, J. Xiao, F. H. Isikgor, Z. Lin, Y. Hao, K. Zeng, Q.-H. Xu, and J. Ouyang, "Enhancing the planar heterojunction perovskite solar cell performance through tuning the precursor ratio," J. Mater. Chem. A **4**, 7943–7949 (2016).

[49]Q. Jiang, L. Zhang, H. Wang, X. Yang, J. Meng, H. Liu, Z. Yin, J. Wu, X. Zhang, and J. You, "Enhanced electron extraction using SnO_2 for high-efficiency planar-structure $HC(NH_2)_2PbI_3$-based perovskite solar cells," Nat. Energy **2**, 16177 (2017).

[50]Q. Meng, Y. Chen, Y. Y. Xiao, J. Sun, X. Zhang, C. B. Han, H. Gao, Y. Zhang, and H. Yan, "Effect of temperature on the performance of perovskite solar cells," J. Mater. Sci.: Mater. Electron. **32**, 12784–12792 (2021).

[51]X. Dong, D. Chen, J. Zhou, Y. Z. Zheng, and X. Tao, "High crystallization of a multiple cation perovskite absorber for low-temperature stable ZnO solar cells with high-efficiency of over 20%," Nanoscale **10**, 7218–7227 (2018).

[52]D. Acuña, B. Krishnan, S. Shaji, S. Sepúlveda, and J. L. Menchaca, "Growth and properties of lead iodide thin films by spin coating," Bull. Mater. Sci. **39**, 1453–1460 (2016).

[53]H. J. Snaith, A. Abate, J. M. Ball, G. E. Eperon, T. Leijtens, N. K. Noel, S. D. Stranks, J. T.-W. Wang, K. Wojciechowski, and W. Zhang, "Anomalous hysteresis in perovskite solar cells," J. Phys. Chem. Lett. **5**, 1511–1515 (2014).

[54]S. Ghosh, R. Singh, A. S. Subbiah, P. P. Boix, I. Mora Seró, and S. K. Sarkar, "Enhanced operational stability through interfacial modification by active encapsulation of perovskite solar cells," Appl. Phys. Lett. **116**, 113502 (2020).

[55]R. T. Ginting, M.-K. Jeon, K.-J. Lee, W.-Y. Jin, T.-W. Kim, and J.-W. Kang, "Degradation mechanism of planar-perovskite solar cells: Correlating evolution of iodine distribution and photocurrent hysteresis," J. Mater. Chem. A **5**, 4527–4534 (2017).

[56]O. V. Oyelade, O. K. Oyewole, D. O. Oyewole, S. A. Adeniji, R. Ichwani, D. M. Sanni, and W. O. Soboyejo, "Pressure-assisted fabrication of perovskite solar cells," Sci. Rep. **10**, 7183 (2020).

[57]A. Guerrero, G. Garcia-Belmonte, I. Mora-Sero, J. Bisquert, Y. S. Kang, T. J. Jacobsson, J.-P. Correa-Baena, and A. Hagfeldt, "Properties of contact and bulk impedances in hybrid lead halide perovskite solar cells including inductive loop elements," J. Phys. Chem. C **120**, 8023–8032 (2016).

[58]O. Almora, I. Zarazua, E. Mas-Marza, I. Mora-Sero, J. Bisquert, and G. Garcia-Belmonte, "Capacitive dark currents, hysteresis, and electrode polarization in lead halide perovskite solar cells," J. Phys. Chem. Lett. **6**, 1645–1652 (2015).

[59]N. K. Tailor, S. P. Senanayak, M. Abdi-Jalebi, and S. Satapathi, "Low-frequency carrier kinetics in triple cation perovskite solar cells probed by impedance and modulus spectroscopy," Electrochim. Acta **386**, 138430 (2021).